Journal of
Materials Chemistry A

ROYAL SOCIETY
OF CHEMISTRY

PAPER

View Article Online
View Journal | View Issue

Check for updates

Cite this: *J. Mater. Chem. A*, 2023, **11**, 1216

Synthesis of platinum nanoparticles on strontium titanate nanocuboids *via* surface organometallic grafting for the catalytic hydrogenolysis of plastic waste†

Katherine E. McCullough,[a] Ian L. Peczak,[b] Robert M. Kennedy,[ab] Yi-Yu Wang,[c] James Lin,[d] Xun Wu,[cd] Alexander L. Paterson,‡[d] Frédéric A. Perras,[d] Jacklyn Hall,[a] A. Jeremy Kropf,[a] Ryan A. Hackler,[a] Youngho Shin,[e] Jens Niklas,[a] Oleg G. Poluektov,[a] Jianguo Wen,[*f] Wenyu Huang,[*cd] Aaron D. Sadow,[*cd] Kenneth R. Poeppelmeier,[*b] Massimiliano Delferro[*ag] and Magali S. Ferrandon[*a]

$Pt/SrTiO_3$ (Pt/STO), prepared on small scale by atomic layer deposition (ALD), is a capable heterogeneous catalyst for the selective hydrogenolysis of polyolefins to hydrocarbon oils, providing a promising approach for upcycling plastic waste. However, because deposition by ALD is costly and resource-intensive, a new synthesis of Pt/STO is needed to effectively scale catalyst production and pursue the commercialization of upcycling processes. To that effect, this work details a scalable deposition method for Pt/STO made by surface organometallic chemistry (SOMC) techniques using Pt(II) acetylacetonate or and trimethyl(methylcyclopentadienyl)platinum. The STO support was calcined (550 °C), treated with ozone (200 °C), and finally steamed (200 °C) to afford a clean STO surface populated with only hydroxyl groups. Pt precursors were dissolved in toluene and deposited onto STO. After reduction at 300 °C, the STO support was decorated with 1.0–1.5 nm Pt nanoparticles. The size and loading of these nanoparticles were varied by employing a multi-cycle deposition and oxidation and/or reduction process designed to ALD techniques. These Pt/STO catalysts hydrogenolyzed isotactic polypropylene into liquid products (>95% yield) with average molecular weights of 200–300 Da (∼25 carbon atoms) and narrow size distributions at 300 °C and 180 psi H_2.

Received 17th October 2022
Accepted 8th December 2022

DOI: 10.1039/d2ta08133d

rsc.li/materials-a

Introduction

Single-use plastics constitute an important cornerstone of the current chemical economy because of their wide-ranging use in many critical industrial sectors. As many as 400 million metric tons of plastics are produced globally each year to meet consumer needs in textiles, medical and construction equipment, and food and beverage products, among other uses.[1–6] Modern society lacks the infrastructure to process post-consumer plastics efficiently and economically, meaning that up to 80% of these products are discarded to landfills. A minority of plastic waste is downcycled, *via* traditional mechanical recycling, which prevents recovery of their inherent chemical value.[4,5] While several chemical recycling approaches have been proposed, there are barriers to their broad implementation at scale. For example, pyrolysis, a high-temperature (∼500 °C) decomposition process in an oxygen-free environment, can successfully break down plastics at various industrial scales but it (1) is inherently unselective and tends to afford wide product distributions, and (2) the value of these products is intimately related to the current price of crude oil, which limits the process' economic upside.[7–10] Overall, developing an economically viable method for chemical recycling will require a process that selectively creates value-added products across a wide range of starting plastics. Ideally, these chemical upcycling techniques should simultaneously recoup the inherent

---

[a] *Chemical Sciences and Engineering Division, Argonne National Laboratory, Lemont, Illinois 60439, USA. E-mail: delferro@anl.gov; ferrandon@anl.gov*

[b] *Department of Chemistry, Northwestern University, Evanston, Illinois 60208, USA. E-mail: krp@northwestern.edu*

[c] *Department of Chemistry, Iowa State University, Ames, Iowa 50011, USA. E-mail: whuang@iastate.edu; sadow@iastate.edu*

[d] *U.S. DOE Ames National Laboratory, Ames, Iowa 50011, USA*

[e] *Applied Materials Division, Argonne National Laboratory, Lemont, Illinois 60439, USA. E-mail: jwen@anl.gov*

[f] *Center for Nanoscale Materials, Argonne National Laboratory, Lemont, Illinois 60439, USA*

[g] *Pritzker School of Molecular Engineering, University of Chicago, Chicago, Illinois 60637, USA*

† Electronic supplementary information (ESI) available. See DOI: https://doi.org/10.1039/d2ta08133d

‡ Present address: National Magnetic Resonance Facility at Madison, University of Wisconsin-Madison, Madison, Wisconsin 53706, USA.

chemical value built into single-use plastics and create a uniform product that can meet a particular commercial need.

At the laboratory scale, a promising upcycling technology is catalytic hydrogenolysis, in which waste polyolefins are selectively converted into liquid and wax-like products using metal nanoparticle catalysts deposited on a metal oxide support.[11–19] We have previously reported such a system in which platinum (Pt) on $SrTiO_3$ nanocuboid (STO; Pt/STO) catalysts convert various high-density polyethylene, low-density polyethylene, polypropylene, and waste plastic streams into highly uniform liquid and waxlike lubricant products with 60–80 carbon atom backbones.[18–21] Recent efforts to model a conceptual pilot plant for this process have shown that Pt/STO upcycling at a scale of 250 Mt day^{-1} could profitably generate lubricant materials while reducing process emissions relative to current industrial methods.[22] These results incentivize further study of Pt/STO upcycling, part of which involves scale-up of Pt/STO catalyst synthesis to the kilogram and ton scales. STO nanocuboids have also previously been investigated as a model catalyst support, and as a bridge between templates for surface science studies and performance-oriented, high surface area supports, and the work developed here may also affect innovation of other M/STO catalyzed processes.[18,19,23–26]

Scaling up the Pt/STO synthesis will require establishing new procedures for support synthesis and Pt deposition. We have previously explored such methods for the scale-up of the STO synthesis, demonstrating that 20+ g of support can be synthesized in a 4 L batch reactor without significant changes to support physical properties nor impact on products of hydrogenolysis when used in a final Pt/STO catalyst.[19] Currently, Pt nanoparticles are introduced onto STO supports *via* atomic layer deposition (ALD), a well-established technique that deposits metals from a gaseous precursor in a precise fashion.[18,23] This process, however, requires highly specialized instrumentation, making it difficult to increase output beyond the gram scale in a short period of time. It is, therefore, necessary to develop a Pt deposition method that retains the precision and tunability of ALD while also facilitating an increase in the output of Pt/STO. Such a deposition method would likely be based on a solution-phase process. Several types of solution-based processes are attractive alternatives to ALD and have found applications in numerous areas of industrial importance not limited to waste plastic upcycling.[27,28]

Solution atomic layer deposition (sALD) is one attempt to develop such a process. Starting from dissolved metal precursors, sALD proceeds *via* the same surface-limited chemistry as conventional, vapor-phase ALD, but improves on the process by both increasing deposition yield and eliminating the need for precursors that are stable in the vapor phase, which are often prohibitively expensive.[29–31] Several sALD systems have been reported for the deposition of inorganic and organic thin films on common metal oxide supports (*e.g.* titania, silica), among other exploratory examples.[29–33]

Another promising synthetic method analogous to ALD is surface organometallic chemistry (SOMC), in which organometallic precursors are chemisorbed onto catalyst support surfaces.[34] Straddling homogeneous and heterogeneous catalysis, this technique generates supported catalysts with single, well-defined active sites without uncontrolled deposition and molecular degradation.[34–37] These active sites also lend themselves well to spectroscopic and kinetic characterization, facilitating the optimization of activity and selectivity.[34] Unlike ALD, SOMC is also scalable and an appealing target for large-scale catalyst deposition.

In the last forty years, SOMC-derived supported catalysts have been tuned through precursor engineering and support control to optimize catalyst activity and selectivity for processes as wide-ranging as metathesis, polymerization, hydrogenation, and hydrogenolysis, among others.[34–39] These works largely focus on grafting onto amorphous silica, a support that is desirable because of its high surface area and high density of surface hydroxyls available for bonding. Many seminal SOMC systems have been developed around early transition metal (*e.g.*, Ti) complexes. Late transition metals form weaker M–O bonds relative to early transition metals, and under hydrogen treatment during SOMC form metal nanoparticles on the catalyst surfaces.[34] For example, SOMC-derived Cu/ZrO_2 catalysts have shown selectivity for the conversion of carbon dioxide to methanol. This selectivity is partially attributed to the activation of CO_2 *via* interaction with Zr(IV) Lewis acid sites in close

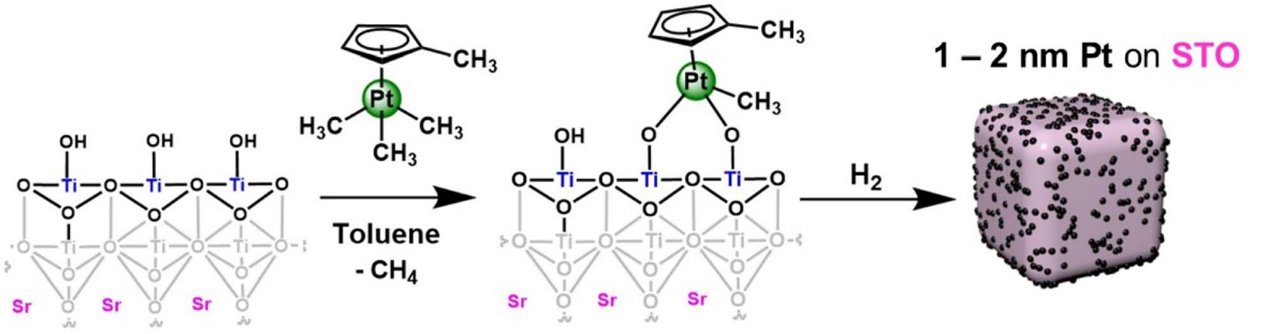

Fig. 1 Stepwise SOMC synthesis of Pt/STO catalysts. Pt (green) is deposited onto a STO nanocuboid (surface termination shown) in toluene under heating *via* trimethyl(methylcyclopentadienyl)platinum(IV) ($MeCpPtMe_3$). $MeCpPtMe_3$ bonds to hydroxyl groups on the STO surface, at which point the sample is placed in a reducing environment ("H_2") to afford a sample with 1–2 nm Pt nanoparticles on the STO nanocuboid support (right).

proximity to deposited Cu particles. Importantly, an SOMC-derived synthesis is integral to this mechanism since it allows for the introduction of highly dispersed and isolated Zr(IV) sites.[34] Comparable activity has been shown for Cu/Ti@SiO_2, whose SOMC synthesis affords a high density of Ti(IV) isolated sites. SOMC techniques have also been used to synthesize PtGa@SiO_2 alloyed nanoparticles, which show high selectivity for alkane dehydrogenation. Additionally, high-throughput screening techniques have been used to synthesize >100 possible SOMC catalysts for testing in dry reforming of methane.[40] Together, these results show that SOMC can produce small, supported nanoparticles for catalysis, with the potential to synthesize a broad range of bimetallic systems.[34]

In this work, we report the synthesis of a supported platinum nanoparticle catalyst *via* SOMC grafting onto STO nanocuboids (Fig. 1 and S1†). We have studied surface treatment *via* calcination, ozonolysis, and steaming of the STO nanocuboids to influence surface hydroxyl density and clean the STO surface. The rationale for using this pre-processing method is consistent with other studies of analogous zeolite supports in which pre-reaction processing influences reaction selectivity.[41–46] Then, the SOMC grafting of Pt precursors was studied, along with chemical treatments to generate Pt nanoparticles from the SOMC materials. All Pt/STO catalysts prepared in these ways were investigated in hydrogenolysis of isotactic polypropylene to provide liquid products with narrow dispersity, replicating the outcomes from ALD materials.

Experimental

Materials

Isotactic polypropylene (i-PP), number-averaged molecular weight (M_n) = 5000 Da, weight-averaged molecular weight (M_w) = 12 000 Da, was obtained from Sigma-Aldrich and used as received.

Synthesis of $SrTiO_3$ nanocuboids

The procedure for the synthesis of large-scale STO nanocuboids was reported by Peczak *et al.*[19] The solution concentrations were proportionally scaled for a 4 L reactor, with the concentrations of Sr, Ti, and NaOH halved relative to the liquid volume to decrease the concentration of chloride ions in the unlined Hastelloy C-276 reactor. Solution A was prepared with 38.69 g of $Sr(OH)_2 \cdot 8H_2O$ dissolved in a solution of 48.04 g of acetic acid and 640.00 g of H_2O under stirring for 2 h. A solution B was prepared with 27.62 g of $TiCl_4$ dissolved in 504.96 g of ethanol for 10 min. The two solutions A and B were mixed and stirred for 10 min in a 2000 mL Erlenmeyer flask; 276.85 g of 10 M NaOH solution was injected into the AB solution for 28 min at a flow rate of 10 mL min^{-1} using a syringe pump. The AB–OH solution was stirred using a magnetic stirrer at the maximum stir rate of the stir plate; no gelation was observed. After mixing and stirring, the AB–OH solution was allowed to sit for 10 min; the pH of the solution was 13.0, and sedimentation occurred.

The solution and sediment were transferred to a 4 L Hastelloy C-276 reactor with an internal impeller and a heating jacket. The reactor was heated to 240 °C at a rate of 2 °C min^{-1} and held for 2 h with a stir speed of 400 rpm. After the reaction, the reactor was cooled at a rate of 2 °C min^{-1}. The precipitate and liquid were transferred from the reactor to a secondary container. The solution pH was 13.2 after the hydrothermal reaction. Initially, the liquid was a light-yellow color but changed to dark orange with time. The precipitate was washed with vacuum filtration and dried in air overnight (12 h, 110 °C).

Treatments of $SrTiO_3$ nanocuboids

Prior to Pt deposition, STO supports were treated through a mixture of calcination in air, ozonolysis, and steaming. STO nanocuboids (~300 mg at a time) were calcined in air between 350 °C and 550 °C for 4 h. STO samples were then introduced into a fixed bed flow reactor and treated with a flow (400 sccm) of ozone in oxygen (8% O_3) using an ozonolyzer (Pacific Ozone, Evoqua Water Technologies LLC) at a constant temperature (200 °C) for 2 h. Samples were then treated with steam at 200 °C for 2 h.

Deposition of Pt onto STO nanocuboids

Vacuum-dried STO nanocuboids (200 °C, 12 h) were suspended in a solution of trimethyl(methylcyclopentadienyl)platinum(IV) ($MeCpPtMe_3$) (Sigma Aldrich, 98%) or platinum(II)acetylacetonate ($Pt(acac)_2$) (Sigma Aldrich, >99.98%) in toluene (target 2 wt% Pt) at various temperatures for 72 h under an inert atmosphere in a N_2-filled glovebox, washed and filtered three times with toluene and once with pentane to remove physisorbed precursor, and then vacuum dried at 60 °C overnight. The sample was either calcined at 300 °C in air for 4 h, and/or reduced under 10% hydrogen at 300 °C for 4 h. In order to increase the amount of Pt loaded onto the STO surface, a multi-cycle (*i.e.* multiple cycles of deposition and reduction) approach was implemented. In a one-cycle (1c) deposition and reduction process, STO samples were introduced into a toluene solution for Pt metalation and then reduced to afford metal Pt nanoparticles as above. The reduction treatment of the ligated Pt/STO catalyst regenerates surface hydroxyls, which creates more available sites for deposition and removes any ligands bound to the Pt metal. Afterward, the 1c-sample was vacuum dried (200 °C, 12 h) and reintroduced into a glovebox to be used for an additional round of deposition and reduction to give the two-cycle (2c) sample. Repeating this process again produced the three-cycle (3c) sample.

Characterization

Nuclear magnetic resonance (NMR) titration. STO samples were introduced into a solution with an excess of $MgBn_2(THF)_2$ (synthesized as reported by Schrock[47]) and a cyclohexane internal standard (C_6H_6, Sigma-Aldrich-Millipore, 99%, A.C.S. reagent) allowed to react in a J-Young tube while being processed on a 500 MHz Bruker NMR spectrometer with multinuclear broadband observe probes (2.5, 5, or 10 mm tube diameter). OH^- site density was calculated through the integration of toluene peaks relative to the cyclohexane standard. Calculation of the absolute amount of toluene in each sample was then taken as a measure of the absolute number of hydroxyls on the STO surface and used to determine mmol of OH per square nanometer of support.

NMR characterization. Solution NMR experiments were conducted using a Brucker UltraShield AVANCE 600 MHz spectrometer ($^1H = 600$ MHz) and spectra were analyzed using MestReNova (v14.1.1-24571). NMR analysis of i-PP derived liquid samples were carried out in 1,1,2,2-tetrachloroethane-d_2 at 395 K (122 °C).

Dynamic nuclear polarization (DNP)-enhanced ^{17}O solid-state NMR experiments were carried out on the bare STO nanocuboids to characterize their surface termination. STO materials were surface-enriched with ^{17}O by first partially dehydroxylating them at 300 °C overnight, rewetting them with 40% ^{17}O-water in a dry atmosphere, and then removing excess water at room temperature under vacuum overnight. This process partially exchanges oxide and hydroxide centers from the surface. The procedure was repeated to surface ^{17}O-enrich a sample of anatase titania that was used as a reference. The material was then wetted with a 16 mM solution of the TEKPol biradical polarizing agent in either fully protonated or fully deuterated 1,1,2,2-tetrachloroethane (TCE),[48] packed into a 3.2 mm sapphire rotor, and inserted into the pre-cooled (100 K) low-temperature MAS probe installed from a Bruker AVANCE III 400 MHz/263 GHz MAS-DNP spectrometer. Measurements were carried out using three approaches, namely, (1) a $^{17}O\{^1H\}$ PRESTO-II experiment excites exclusively hydroxyl ^{17}O species,[49,50] (2) a $^{17}O\{^1H\}$ D-RINEPT-$SR4_1^2$(tt) experiment excites both hydroxyls and oxide ^{17}O centers that are near ^1H nuclei,[51] and (3) a ^{17}O direct DNP experiment that reveals all surface ^{17}O centers,[52] regardless of ^1H locality. The MAS spinning frequency was set to 13.888 kHz and ^{17}O pulses utilized effective RF powers of 25 kHz. ^1H RF powers were of 100 kHz for hard and CW pulses and 132 kHz for the tanh/tan adiabatic $SR4_1^2$ pulses used in the D-RINEPT-$SR4_1^2$(tt) experiments. Recycle delays were set to 2 s and 8 s for the indirect and direct DNP experiments performed on the STO, respectively, and 10 s in the case of anatase TiO_2. Quadrupolar Carr–Purcell Meibook–Gill (QCPMG) was applied for sensitivity enhancement.[53] 34 echoes were acquired, with a spikelet separation of 694 Hz. PRESTO spectra were acquired in 2048 and 768 scans for STO and TiO_2, respectively, with 2 rotor cycles of recoupling and INEPT spectra were acquired in 8192 and 1536 scans with 32 rotor cycles of recoupling. Direct DNP experiments utilized a 6.94 kHz spikelet separation, recycle delays between 1 and 256 s and acquired in 256 scans. Through-space $^{17}O\{^1H\}$ heteronuclear correlation experiments were measured using the D-RINEPT-$SR4_1^2$(tt) pulse sequence and 100 kHz ^1H frequency-switched Lee-Goldburg homonuclear decoupling.[54] 672 scans were acquired for each of the 16 t_1 increments of 130.672 μs and the QCPMG spikelet separation was increased to 2.315 kHz.

$^1H\{^{195}Pt\}$ experiments were carried out using a sideband-selective perfect-echo (PE)-RESPDOR experiment using an Agilent DD2 400 MHz spectrometer equipped with a Samoson 1.7 mm fast-MAS probe.[55] Samples were packed into 1.7 mm rotors in an inert atmosphere and spun to 40 kHz using pressurized nitrogen. Hard ^1H pulses utilized a 100 kHz RF field while the sideband-selective, 50 μs, ^{195}Pt pulses were applied with a 13 kHz RF power. The total recoupling time was equal to 1.2 ms. Sub-spectra were acquired in either 2048 or 16 384 scans with a 1 s recycle delay. The ^{195}Pt offset frequency was first stepped in 10 kHz increments around −2000 ppm to find a spinning sideband and was then stepped in 40 kHz increments to measure the intensities of the neighboring spinning sidebands.

Density functional theory. Density-functional theory (DFT) calculations of ^{17}O magnetic shielding and electric field gradient tensors were carried out using CASTEP (version 2018).[56] The default "on-the-fly" ultrasoft pseudopotentials were used together with the exchange-correlation functional of Perdew, Burke, and Ernzerhof (PBE).[57,58] Structures were first geometry optimized with convergence tolerances of 2×10^{-5} eV per atom in total energy, 0.05 eV $Å^{-1}$ in forces, and 0.002 Å in maximum atomic displacement. Geometry optimization calculations used kinetic energy cutoffs of 489.8 eV, a *k*-point grid density of 0.08 $Å^{-1}$, and the Grimme D2 dispersion scheme.[59] Shielding calculations used the gauge-including projector augmented-wave (GIPAW) method as implemented within CASTEP.[60,61] The kinetic energy cutoff was increased to 700 eV and the *k*-point grid density was set to 0.03 $Å^{-1}$. ^{17}O magnetic shielding constants converged to within 1 ppm and were converted to chemical shifts using a reference shielding of 187.065 ppm calculated using SrO and TiO_2.

Electron microscopy. Nanoparticle imaging was conducted by scanning transmission electron microscopy, using a FEI Talos F200X TEM/STEM operated at 200 kV. Aberration-corrected high-resolution transmission electron microscopic images were acquired using the Argonne Chromatic Aberration-corrected TEM (ACAT), a FEI Titan 80-300 ST with an image corrector to correct both spherical and chromatic aberrations. These microscopes were used in coordination with the Center for Nanoscale Materials (CNM) at Argonne National Laboratory. In preparation for analysis by electron microscopy, powdered samples (∼20 mg) were sonicated in ethanol (10 mL) for 15 minutes. The resulting suspension was dropcast onto a lacey carbon TEM grid (Ted Pella, Inc., UC-A on Lacey 400 mesh Cu). Particle size and shape were measured using ImageJ and Gatan Digital Micrograph software.[62] The face-to-face distance between opposing [100] faces of STO nanocuboids was used as a measure of particle width.

Brunauer–Emmet–Teller (BET) surface area measurements. The catalyst surface area was determined by nitrogen adsorption using a Micromeritics ASAP 2010 instrument. Each sample was degassed by heating at 150 °C under vacuum prior to measuring the surface area. Five data points were measured for an accurate evaluation of surface area.

X-ray absorption fine structure (XAFS). XAFS spectroscopy measurements were completed at the 10ID beamline at the Advanced Photon Source (APS) of Argonne National Laboratory. The beam was generated *via* an undulator source with a liquid N_2-cooled Si(111) double crystal monochromator (DCM) and harmonic rejection mirror. Spectra were collected in fluorescence mode using Soller slits and a Zn filter with a fluorescence ionization chamber. Simultaneous measurement of the Pt foil was completed and calibrated to 11 562.76 eV at the zero-crossing of the second derivative. Samples were diluted with SiO_2 and pressed into self-supporting wafers at a 45° angle and placed within an *in situ* gas cell as described in detail in a previous report.[63a] Spectra were measured under He flow (200 mL min^{-1}) at room temperature before and after reduction (3.5% H_2/He, 250 °C, 10 minutes, 50 mL min^{-1}) to remove surface oxide species formed in the samples upon contact with air. Data processing (includes normalization, background subtraction calibration, and fitting) was performed using the Demeter/Athena/Artemis suite of XAFS analysis software.[63b]

Electron paramagnetic resonance spectroscopy (EPR). Continuous wave (CW) X-band (9–10 GHz) EPR experiments were carried out with a Bruker ELEXSYS II E500 EPR spectrometer (Bruker Biospin, Billerica, MA), equipped with a TE_{102} rectangular EPR resonator (Bruker ER 4102ST). Field modulation at 100 kHz in combination with lock-in detection leads to first derivative-type CW EPR spectra. Measurements were performed at 15 K. A helium gas-flow cryostat (ICE Oxford, UK) and an ITC (Oxford Instruments, UK) was used for temperature control. Data processing was performed using Xepr (Bruker Biospin, Billerica, MA) and MatlabTM R2018b (MathWorks) environment.

Thermogravimetric analysis (TGA). TGA was carried out using a TGA Discovery (TA Instruments) coupled with a mass spectrometer (QMS200, Stanford Research Systems) with 10 mL min^{-1} N_2.

Powder diffraction (PXRD). The crystalline phase compositions of the samples were determined by PXRD using a Bruker Diffractometer D8 Advance operating with the following parameters: Cu Kα radiation of 40 mA, 40 kV, $K_\lambda = 0.15418$ nm, 2θ scanning range of 20–60°, a scan step size of 0.0018° and a time of 1 s per step. The sample was placed on a zero-background silicon holder (MTI Corp.) for analysis.

Inductive coupled plasma (ICP). Metal analysis was performed at the Northwestern University Quantitative Bio-element Imaging Center. Quantification of Pt, Sr, and Ti was accomplished using ICP-OES of acid-digested samples.

Catalytic hydrogenolysis of i-PP using Pt/STO. Hydrogenolysis experiments were performed in 100 mL Parr autoclaves equipped with an overhead stirrer and thermocouple extending to just above the melted polymer. i-PP (3 g) and Pt/STO catalyst (300 mg) were loaded into a glass liner in the reactor. The autoclave was sealed, and then evacuated and refilled with mixed gas (9 : 1 ratio of H_2 : He) three times. The reactor was pressurized with mixed gas (9 : 1 ratio of H_2 : He) at 827 kPa at room temperature, and then heated to 300 °C (1.2 MPa). After 24 h, the reactor was allowed to cool to room temperature. The gas in the headspace was directly injected into a gas chromatograph (GC) for analysis (see below). The remaining gas in the headspace was slowly released. The liquid products were collected and fractionated based on their location either outside the liner (OL) or inside the liner (IL). OL-products were directly collected by pipette, while IL-products were extracted with *n*-hexane (HPLC grade) warmed at 55 °C. The extracted solution was filtered through silica gel, and the solvent was removed using a rotary evaporator. Both OL- and IL-products were analyzed by ultra-high pressure liquid chromatography (UHPLC), NMR, and thermogravimetric analyzer-differential scanning calorimetry (TGA-DSC). In the manuscript, the total amount of liquid is the sum of OL and IL.

Liquid species analysis. A Waters Corporation UHPLC system equipped with the ACQUITY AQT XT45 (1.7 μm, 4.6 mm, 150 mm) analytical column was used to characterize the M_n and M_w of the soluble products. The calibration standard included research-grade, pure alkane species individually (*n*-octane, *n*-nonane, *n*-decane, *n*-dodecane, *n*-hexadecane, *n*-octadecane, *n*-eicosane, *n*-tetracosane, *n*-octacosane, *n*-dotriacontane, and *n*-hexatriacontane, 1 mL, 50 mg mL^{-1}). A calibration curve and representative spectrum are presented in the ESI (Fig. S2†). OL- and IL-products were dissolved in *n*-hexane (1 mL, 50 mg mL^{-1}) and injected for analysis.

Quantification of gas species. The volatile products were sampled by connecting the autoclave to a GC sampling loop and analyzed simultaneously using a GC-flame ion detector (FID) and a GC-thermal conductivity detector (TCD) installed on a HP 5890 gas chromatograph. A Supelco 60/80 Carboxen 1000 (15′ × 1/8″ × 2.1 mm) packed column (GC-TCD) was used to measure the ratio of H_2 to He (internal standard) to quantify H_2 in the headspace after an experiment. An Agilent GS-Gaspro (15 m × 0.32 mm × 0.00 μm) capillary column was used to separate and quantify the C_1–C_9 hydrocarbon species by GC-FID. Quantification of volatile hydrocarbons was conducted by using a calibrated gas tank (Matheson, C_1–C_4 hydrocarbons gas tank) and pure small molecular weight alkanes solvent vapor (Sigma-Aldrich, HPLC grade, *n*-pentane, *n*-hexane, *n*-heptane, and *n*-octane). A graphical display of a calibration curve is presented in the ESI (Fig. S3†).

TGA-DSC analysis. i-PP derived samples were analyzed simultaneously by TGA and DSC configuration, installed on a Netzsch (STA 449F1) equipped with Al_2O_3 crucible (volume 85 μL) with lid. The instrument calibrations (weights, temperature, and sensitivity) were performed using calibration sets (serial #14565) provided by Netzsch. An empty Al_2O_3 crucible served as reference. A 3 mg sample was placed in the sample crucible, covered by a lid. The sample was heated from 40 to 550 °C with 3 °C min^{-1} in a streaming nitrogen atmosphere (purge: 20 mL min^{-1}; protective: 20 mL min^{-1}) to suppress oxidation. The total instrumental runtime was 3 h. Analysis of DSC peaks was carried out using Proteus Thermal Analysis Software (Ver 8.0.2) from Netzsch.

Results and discussion

Preparation of STO nanocuboids prior to surface modification studies

Strontium titanate ($SrTiO_3$, STO) nanocuboids (nano-rectangular prisms) were synthesized hydrothermally as per the scaled-up method described in Peczak *et al.* at 240 °C for 2 h.[19,64] The STO nanocuboids have an average size of 45 ± 10 nm and an average shape of a cube composed of (100) facets, with rounded edges. 70 to 75% of nanoparticles in the STO sample take this shape, though the batch is 100% crystalline $SrTiO_3$ by powder X-ray diffraction. Previous work has demonstrated that hydrothermally synthesized STO nanocuboids predominantly have a Ti-rich, $\sqrt{13}$ by $\sqrt{13}$, 33.3° rotated TiO_2 double layer reconstruction on the surface of the {100} facets,[19,64–72] and that upon annealing at elevated temperatures, the rounded corners between these {100} facets reform into {110} facets.[66] Additionally, bulk STO has a close lattice match with platinum, which can result in a high degree of epitaxial stabilization of platinum nanoparticles on the support surface.[23,26,73] Previously, platinum nanoparticles with narrow size distribution and a range of sizes were synthesized on STO nanocuboids by atomic layer deposition (ALD).[18,23,25,26,74] These ALD-derived Pt/STO catalysts synthesized show no signs of immediately evident $SrCO_3$ buildup at room temperature or typical reaction conditions (200–300 °C), per results collected *via* X-ray diffraction (Fig. S4†), though some carbonate desorption was observed at high temperatures (Fig. S5†).

In atomic layer deposition, ozone treatment is used to clean the STO surface because as-synthesized STO nanocuboids can have a range of adventitious species on the surface, including hydroxyls as part of the surface termination, adsorbed water, or ions (*e.g.* sodium, chloride, hydroxide, acetate, carbonate) from the hydrothermal solution, as suggested in Peczak *et al.*[19] Carbonates, for example, can form during the STO synthesis when inhomogeneity in the pre-heating Sr–Ti–OH mixture creates local environments with intermediate pH (*e.g.* 3 < pH < 9). In this range, strontium carbonate is more thermodynamically stable than strontium titanate.[19,75–77] The concentration of the adsorbed ions from the reaction mixture can be significantly decreased by washing and drying the nanoparticles post-synthesis. However, such post-reaction processing still allows for some species, such as hydroxyls and water, to remain on the surface. Variation in the concentration of hydroxyls and water on the surface, both between batches and between individual cuboids, can result in inhomogeneity in the grafting of catalyst precursors on the surface of the support. To minimize this effect, various pre-treatments can be performed to burn or desorb species on the surface or to selectively re-introduce desired surface species. Here, calcination and ozonolysis were used for the former, and steam for hydroxyls.

Surface modification through calcination

STO nanocuboids were calcined for 4 h at temperatures between 350 °C and 550 °C. Particle size and the relative amount of nanocuboid particles are statistically equivalent in the as-synthesized sample and post-calcination samples (Fig. S6 and

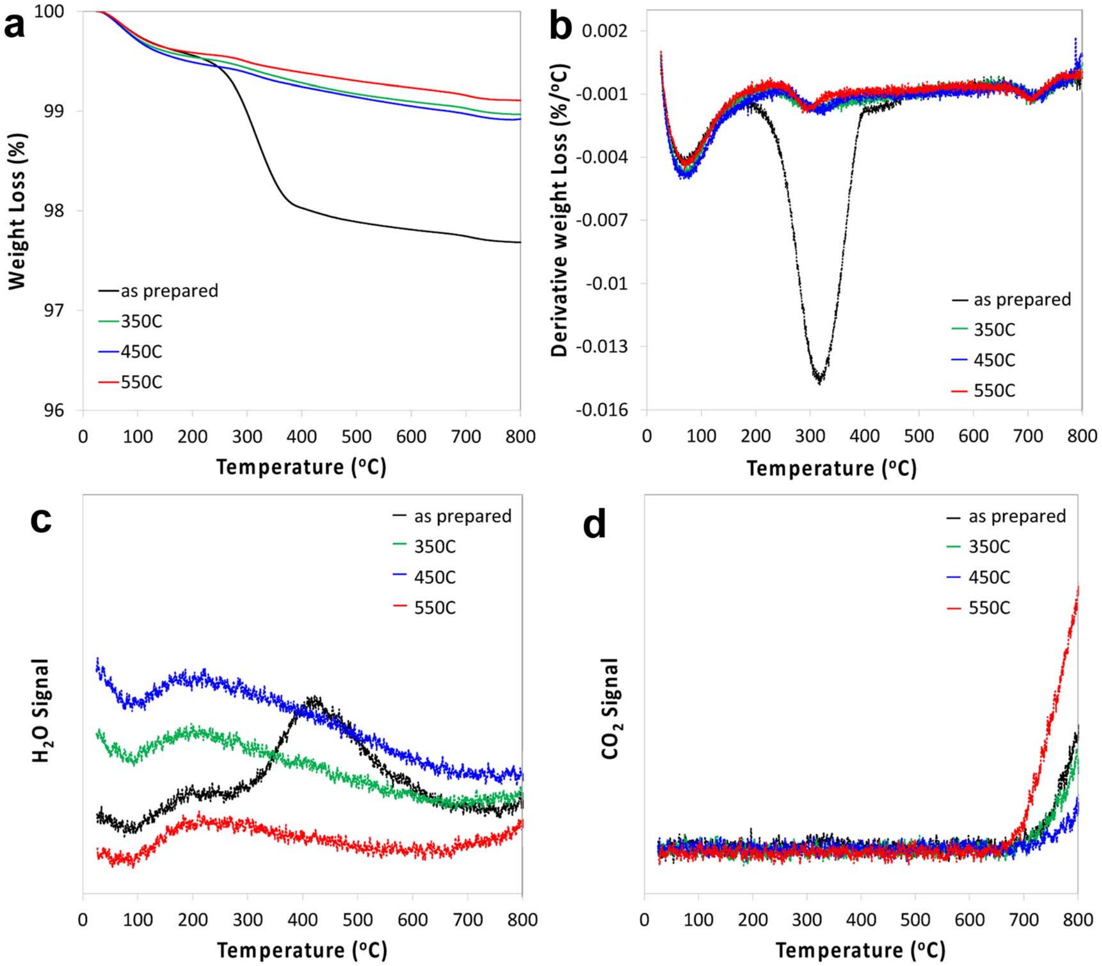

Fig. 2 TGA (a), 1st derivative (b), water signal (c) and CO_2 signal (d) of STO as prepared and after calcination at 350 °C, 450 °C and 550 °C.

Table S1†). Calcination of as-synthesized STO nanocuboids at 350 °C and 550 °C desorbed most surface species, which generally desorb between 200 °C and 600 °C, as seen by TGA of the calcined materials (Fig. 2). These results demonstrate that calcination at 550 °C exhibits the lowest weight loss of desorbed species, indicating that this surface is the least contaminated and therefore cleanest. At around 550 °C, the surface area of the STO sample has decreased 37% from the as-synthesized sample even though particle morphology does not visibly change. This likely stems from the coalescence of individual STO nanocuboids (Table S2†). To avoid this and ensure that the STO support surface area was sufficiently high for catalyst deposition, calcination treatments were not carried out at temperatures higher than 550 °C.

Effect of calcination on $MeCpPtMe_3$ grafting

One cycle of platinum was deposited at room temperature on STO samples calcined at 350 °C or 550 °C, using the $MeCpPtMe_3$, the organometallic precursor used for ALD of Pt, resulting in Pt/STO samples with weight loadings of 0.019 wt% and 0.13 wt%, respectively. It appears that the Pt particle size is uneven on the STO calcined at 350 °C, while it is more uniform when deposited on STO calcined at 550 °C (Fig. 3). Uneven deposition on otherwise equivalent samples is likely due to remaining surface species that interfere with Pt grafting, making calcination at 550 °C the preferred temperature. However, the weight loading of Pt is still low relative to previously reported ALD deposition and can likely be increased through additional pre-deposition surface treatments.

Surface modification through ozonolysis

A similar effect to calcination can be achieved at lower temperatures using stronger oxidants, such as ozone through ozonolysis. The lower temperature of ozonolysis can be beneficial if there are other properties, such as phase transitions or sintering, that would be accelerated at higher temperatures. In this work, both processes were used in sequence to ensure that STO support surfaces were sufficiently clean for Pt deposition. Additionally, because ozone treatment at 200 °C was previously used to deposit Pt by ALD,[18] the use of ozonolysis in this work enables a comparative study between ALD- and SOMC-derived Pt deposition methods. Ozone treatment at 200 °C was used to treat the STO surface after calcination prior to catalyst deposition. Pt deposition was conducted *via* SOMC of $MeCpPtMe_3$ at 65 °C on STO supports treated by both calcination and a combination of calcination and ozonolysis. Ozone treatment did not significantly affect final Pt particle size, as final particle sizes for both samples were 1.3 nm (Fig. 4), and Pt weight loadings were similar (0.13 wt% without ozone and 0.12 wt% with ozone).

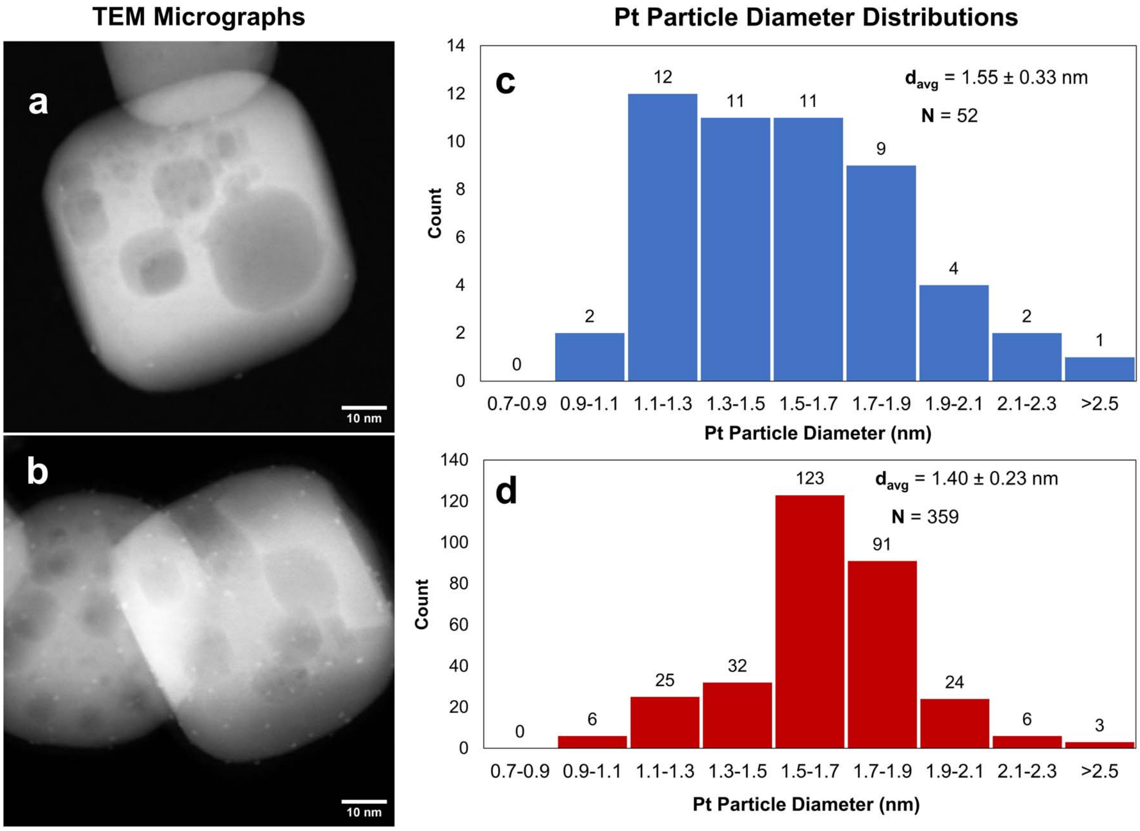

Fig. 3 1cPt/STO using STO pre-calcined at 350 °C (a) and at 550 °C (b). Metalation of $MeCpPtMe_3$ at 25 °C. Pt particle size distributions for the samples presented in (a) and (b) are provided in the adjacent histograms in (c) and (d), respectively.

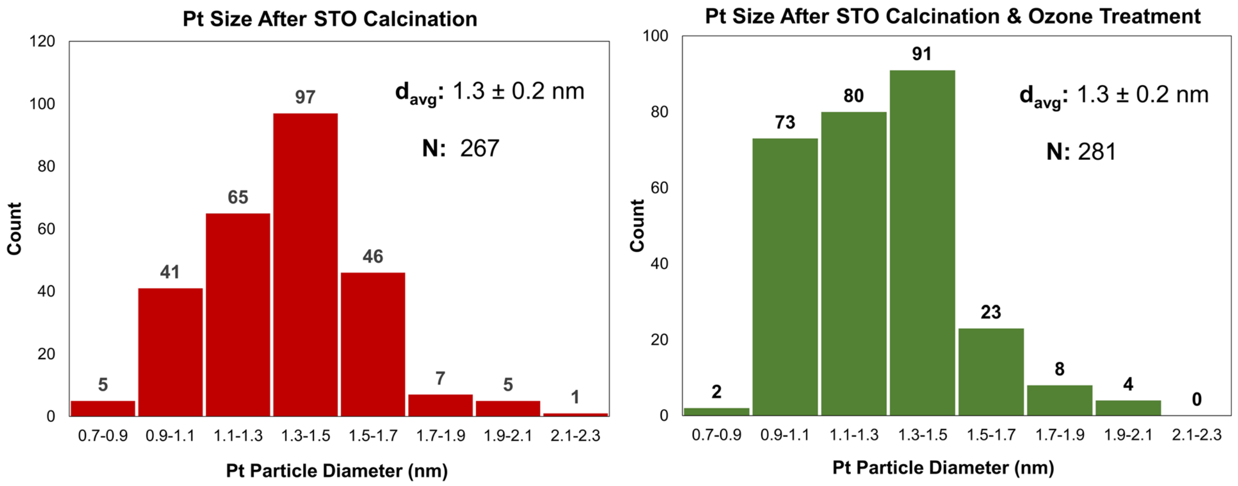

Fig. 4 Platinum particle size distributions for SOMC 1cPt/STO prepared with STO that had been calcined at 550 °C and steamed at 200 °C (red, average size of 1.3 ± 0.2 nm) and with an additional ozone treatment at 200 °C between the calcination and steaming steps (green, average size of 1.3 ± 0.2 nm). Metalation of $MeCpPtMe_3$ at 65 °C.

Effect of steam treatment

Any combination of calcination and ozonolysis likely leads to significant dehydroxylation, meaning that hydroxyls must be replenished prior to SOMC grafting. Steam treatment at elevated temperatures can be used to re-introduce controlled concentrations of surface hydroxyls.[78] NMR titration of surface hydroxyls on STO nanocuboids with $Bn_2Mg(THF)_2$ on samples calcined at 550 °C and then steam-treated at temperatures ranging from 100 °C to 500 °C revealed that the hydroxyl concentration reaches a maximum of 17.3 OH per nm^2 at 200 °C (Fig. S7†). The presence of O_3 did not significantly affect surface hydroxyl concentrations. Below that temperature, the number of reconstituted hydroxyls is low, and above that temperature, the formation of hydroxyls is increasingly in competition with the reverse dehydration reaction to form a bridging oxygen, shifting the equilibrium toward low hydroxyl concentrations.[79a,b] Steam treatment at 200 °C was selected to use as a post-treatment of ozonolysis. TGA confirms a higher loss of water when ozone is used in between the calcination at 550 °C and the steam treatment at 200 °C (Fig. S8†). It is likely that the increased oxidizing power of ozone is leading to re-arrangement and stabilization of the surface, making it more prone to reaction with water to form hydroxyls.

DNP-enhanced ^{17}O solid-state NMR was carried out to characterize the structure of the formed hydroxy species and surface termination. Three experiments, PRESTO, D-RINEPT-$SR4_1^2$(tt), and direct DNP, were conducted to selectively detect hydroxyl species, all oxygen centers near ^1H spins, and all oxygen centers regardless of environment, respectively. The D-RINEPT-$SR4_1^2$(tt) experiment revealed two major surface environments resonating near 500 and 100 ppm at 9.4 T, the later of which could be assigned to hydroxyls using the PRESTO measurement (Fig. 5). Plane-wave DFT calculations were carried out on the $c(4 \times 4)$[80] and $(\sqrt{13} \times \sqrt{13})R33.7°$ terminations of STO,[81] in addition to three hydrated variants of the (2×1) termination,[82,83] to predict the ^{17}O chemical shifts and quadrupolar coupling parameters for various surface environments. These calculations revealed that the signal around 500 ppm can be attributed to surface oxygen species in the TiO_2 double layer, with potentially a shoulder from the Sr layer. No evidence for Sr–OH species was detected, meaning that, as expected, the Pt grafting sites are Ti–OH species. The ratio of the Ti–O–Ti and Ti–OH signal intensities was similar in a direct DNP experiment and was not affected by the solvent protonation level. $^{17}O\{^1H\}$ HETCOR experiments revealed that the major correlation for the oxide resonances was from a neighboring Ti–OH species, and this was not affected by the application of a longer recoupling time in protonated TCE (*i.e.* no correlations to solvent were observed, Fig. 5). This indicates that hydroxyls are found homogeneously on all STO facets and that significant defects are present in the usually hydrophobic $(\sqrt{13} \times \sqrt{13})R33.7°$ surfaces, in agreement with the high average hydroxyl density.

Effect on Pt precursor and solution temperature on grafting

The amount of Pt loading *via* SOMC can be increased by changing the starting Pt complex that is grafted to the STO surface. $Pt(acac)_2$ and $MeCpPtMe_3$ are two common platinum precursors used in catalyst synthesis.[82–85] In addition to traditional methods such as wet impregnation, incipient wetness, and co-precipitation, these precursors have been used for ALD of Pt nanoparticles on oxide surfaces,[86] with $MeCpPtMe_3$ specifically used to grow Pt nanoparticles of a range of sizes through cyclic growth on STO nanocuboids.[18,23,24,26,86] On STO calcined at 550 °C, ozone and steam treated at 200 °C, grafting at 50 °C of $Pt(acac)_2$ was more efficient (0.50 wt% Pt) than the grafting using $MeCpPtMe_3$ (0.12 wt%), which is expected due the covalent nature of the Pt–C bond in the latter.

Solid-state NMR $^1H\{^{195}Pt\}$ perfect-echo RESPDOR experiments (Fig. 6) were performed on a sample of $MeCpPtMe_3$ grafted onto STO. Correlations were observed in the sideband-

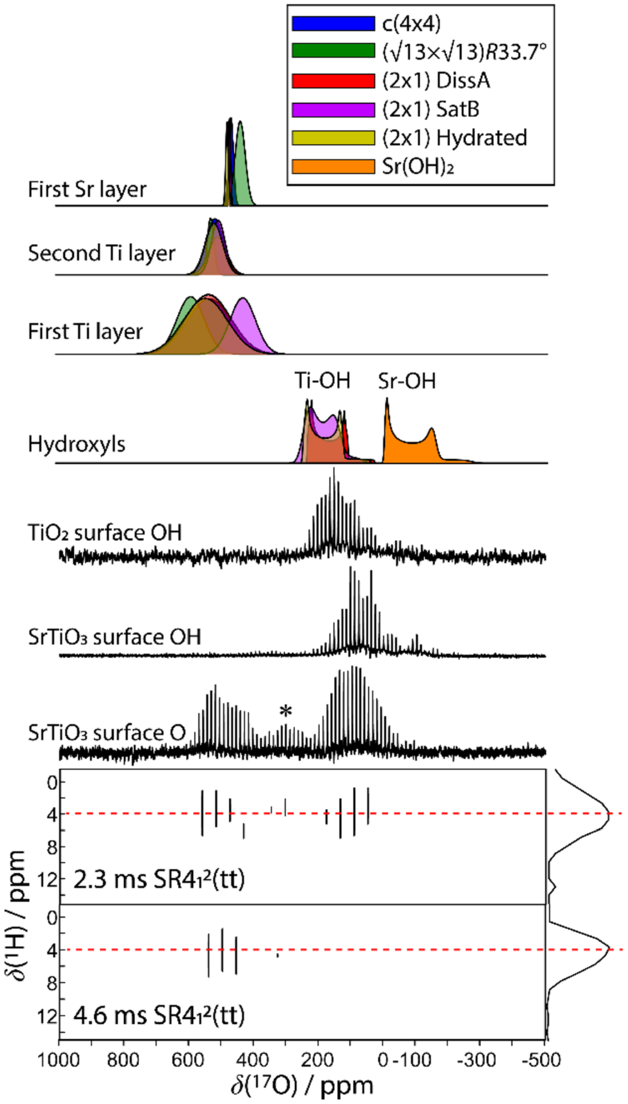

Fig. 5 Experimental (black) D-RINEPT-SR4_1^2(tt) (bottom) 1D and 2D^{17}O{^{1}H} spectra and ^{17}O{^{1}H} PRESTO spectra acquired on STO and anatase titania. Simulated spectra are shown on the top corresponding to the parameters calculated using plane-wave DFT for various surface terminations, as indicated on the figure. An asterisk is used to mark the position of a spinning sideband.

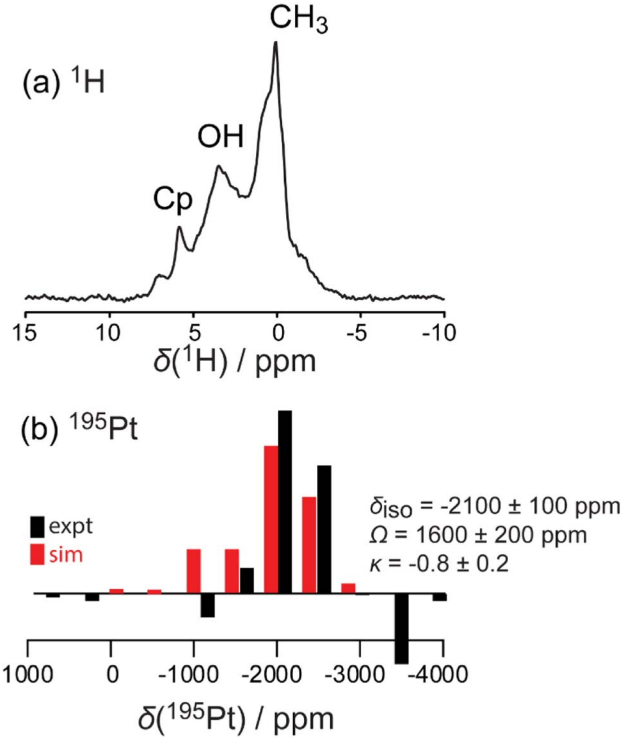

Fig. 6 Simulated (red) and experimental (black) ^{1}H MAS (a) and ^{1}H{^{195}Pt} perfect-echo RESPDOR (b) solid-state NMR spectra acquired on a MeCpPtMe$_3$/STO material.

selective experiment corresponding to a uniform Pt environment characterized by an isotropic ^{195}Pt chemical shift of −2100 ± 100 ppm, a tensor span of 1600 ± 200 ppm, and a skew of −0.8 ± 0.2. These parameters are similar to those measured in a MeCpPtMe$_3$/Zn–SiO$_2$ catalyst,[87] suggesting that it adopts a similar bipodal coordination environment. This is consistent with the observation that after grafting of MeCpPtMe$_3$ onto STO supports, the final Pt loading (0.5 wt%) was lower than that obtained with Pt(acac)$_2$ (2 wt%), as a bipodal mode of grafting consumes surface hydroxyls that would otherwise be available for additional Pt deposition. No evidence of monopodal or tripodal Pt species was detected.

EPR spectroscopy confirmed the presence of Ti(III) on STO both as synthesized and after calcination (Fig. S9†). The observation of Ti(III) in these samples is consistent with previous reports that show Ti(III) evolution in STO after treatment in both reducing environments and high-temperature annealing environments. It has been proposed that such an environment can introduce oxygen vacancies into the STO crystal lattice, leading to a reduction of Ti^{4+} to Ti^{3+} to preserve electrical neutrality.[87–89] Overall, Ti(IV) appears to be the dominant Ti species, though paramagnetic effects from Ti(III) overwhelm the NMR signals for ^{1}H and ^{195}Pt.

Metalation temperature for Pt(acac)$_2$ deposition

After STO nanocuboids were calcined at 550 °C and treated by ozonolysis and steaming (both at 200 °C), Pt(acac)$_2$ was grafted onto the STO nanocuboids in toluene at temperatures ranging from 50 °C to 120 °C for 72 h. The Pt loading was slightly affected by solution temperature for Pt(acac)$_2$, with 0.50 wt% Pt deposition being observed at 50 °C, and increasing slightly to 0.54 wt% at 80 °C and 0.55 wt% at 120 °C (Fig. 7). A metalation temperature of 90 °C was also tested, and average Pt particle size was comparable to that observed for depositions carried out at 80 °C (Fig. S10†). A metalation temperature of 120 °C led to larger particles, however, which are thought to be less active for polyolefin hydrogenolysis.[18] Thus, metalation at 80 °C was selected for further experiments.

Multiple-cycle deposition

One of the unique features of the self-limiting ALD processes is that particles or layers of a desired size or thickness can be

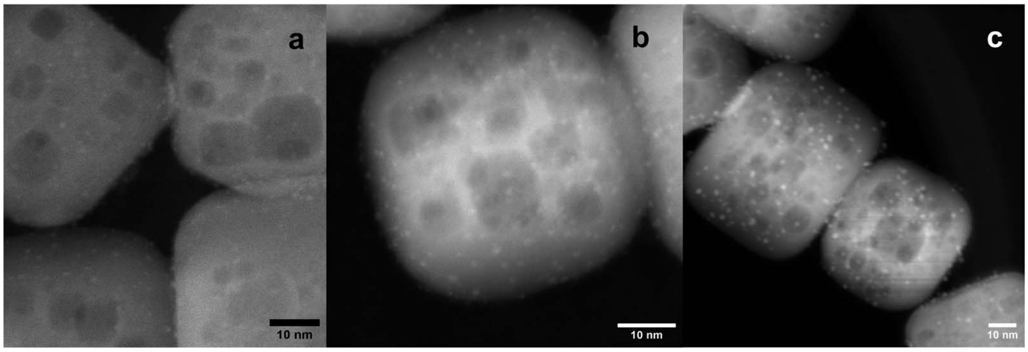

Fig. 7 STEM HAADF micrographs of SOMC 1cPt/STO calcined at 550 °C, followed by O_3 and steam treatment at 200 °C, made at a 50 °C (1.2 ± 0.3 nm; (a)), 80 °C (1.3 nm, (b)), and 120 °C (1.8 nm, (c)).

grown by repeating the growth cycle a specific number of times.[23,90] SOMC is also a self-limiting deposition process, and it should be possible to perform additional cycles of grafting to deposit controlled amounts of Pt on the surface until a desired particle density or size is reached. We observed the Pt surface loading increase from 0.90 Pt atoms per nm^2 after one cycle to 1.66 Pt atoms per nm^2 after two cycles. Interestingly, the average Pt nanoparticle diameter was independent of the number of cycles at 1.3 ± 0.3 nm, 1.2 ± 0.39 nm, and 1.5 ± 0.35 nm after the 1, 2, and 3 cycles (Table 1). Instead, increases in Pt loading are driven by new nanoparticle formation. The cycle-by-cycle growth behavior of SOMC under reducing conditions is different from analogous ALD depositions, where oxidizing conditions appear to favor particle growth over new nucleation on subsequent cycles.[86,90]

After the Pt precursor is grafted to the STO nanocuboid surface (two cycles), the excess precursor is washed off with toluene and the pre-catalyst is dried before forming Pt nanoparticles. Like ALD,[86] Pt nanoparticles can be formed *via* oxidation or reduction of the grafted species to remove the stabilizing ligands. In both the oxidizing and reducing cases, the individual Pt atoms are mobile on the oxide surface and nucleate to form nanoparticles. In the case of ALD at sub-atmospheric pressures, under oxidizing conditions, PtO_x/Pt^0 core–shell particles form, while a metallic Pt^0 particle forms under reducing conditions.[86,90] The mobility of the Pt species can be modified by adjusting the partial pressure of the oxidant or reductant.[85] Here, the grafted Pt species were either annealed under air at 300 °C, or reduced under hydrogen at 300 °C for 4 h, or annealed at 300 °C under air followed by reduction at 300 °C for 4 h. An annealing temperature of 300 °C was chosen to remove organics according to TGA (Fig. S11†). The average particle sizes and distributions for all three conditions are summarized in Fig. 8 and Table 1 along with the Pt loadings. Oxidizing before reducing lowers the average Pt particle size from 1.2 to 1.0 nm compared to reduction only, indicating that PtO_x may be better stabilized onto STO, also shown by the Pt/Ti ratio of 0.374 that remains constant after reactions. The higher Pt/Ti ratio in the reduced sample only may be due to the higher reduction of Pt species compared to the calcined and reduced samples (Fig. 8 and Table 1). A layer of PtO_x in contact with the support would favor stronger binding compared to Pt^0.[90,91]

Both Pt/STO catalysts mentioned in Fig. 8 were examined by high-resolution transmission electron microscopy (HRTEM) to examine the interface between the Pt catalyst and STO support. The results are presented below in Fig. 9. These micrographs demonstrate cube-on-cube epitaxy between the Pt metal {100} facet and {100} STO support facet. However, planar epitaxy between the Pt metal {101} facet and the {100} facet was observed in some images. Image analysis suggests that the epitaxy shown in Fig. 9 represents a minor portion of all Pt/STO catalyst–support interactions. This epitaxial stabilization is likely responsible for the high stability of deposited Pt nanoparticles against sintering. Although previous reports of Pt/STO

Table 1 Average Pt particle size, measured from STEM-HAADF images, and loadings measured by ICP. Pt particle size ranges estimated from EXAFS fit results from Table 2 (see below). STO calcined at 550 °C followed by O_3 and H_2O at 200 °C. Metalation of $Pt(acac)_2$ at 80 °C

	Average diameter ± SD (nm)	Particle range[a] (nm)	Pt loading (wt%)	Pt/Ti
1cPt_red/STO	1.3 ± 0.30		0.562	0.0224
2cPt_red/STO	1.2 ± 0.39	1.3–1.8	1.082	0.0446
3cPt_red/STO	1.5 ± 0.35		1.636	0.0365
2cPt_red/STO_spent	1.8 ± 0.89	1.3–1.9	1.204	0.0443
2cPt_calc/STO	0.8 ± 0.22		0.884	0.0374
2cPt_cal + red/STO	1.0 ± 0.20	1.1–1.9	0.936	0.0374
2cPt_cal + red/STO_spent	1.3 ± 0.49	1.0–1.3	0.960	0.0214

[a] The number of atoms per particle was calculated using estimations described by Jentys[88] and assuming a spherical particle shape.

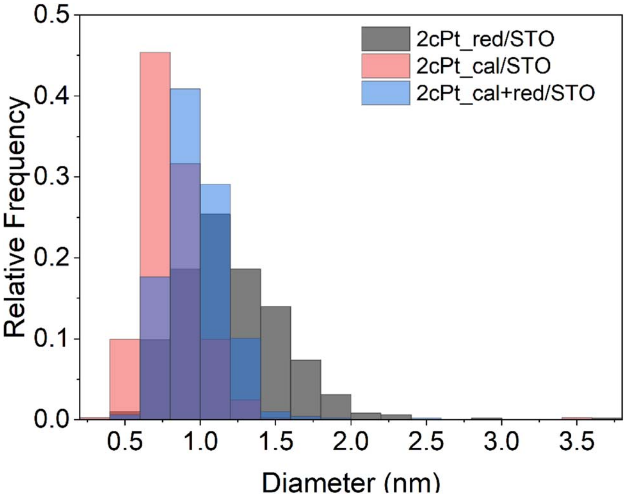

Fig. 8 Pt particle size distribution of 2cPt/STO after calcination, reduction and both oxidation at 300 °C followed by reduction at 300 °C. STO support has been calcined at 550 °C followed by separate O_3 and steam treatment both at 200 °C.

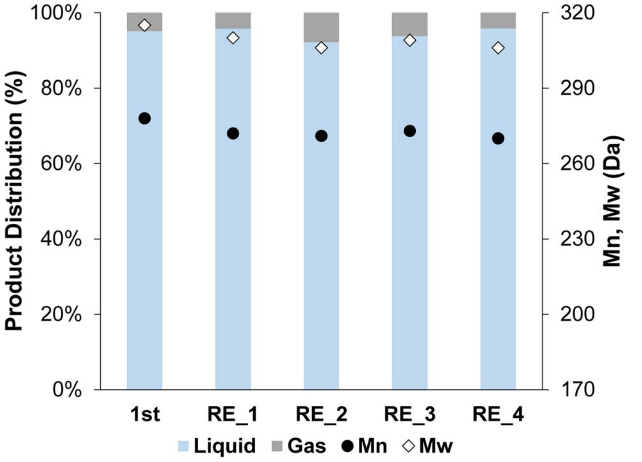

Fig. 10 Product distribution (liquid and gas) and M_n and M_w from OL after the first hydrogenolysis and 4 consecutive recycling experiments using 2cPt_red/STO. Conditions: i-PP (3 g), 301.0 mg 2cPt_red/STO catalyst, 300 °C, 180 psi mixed gas, 24 h. For gas distribution, see ESI.† No solid products were observed. $Đ = 1.1$ for all.

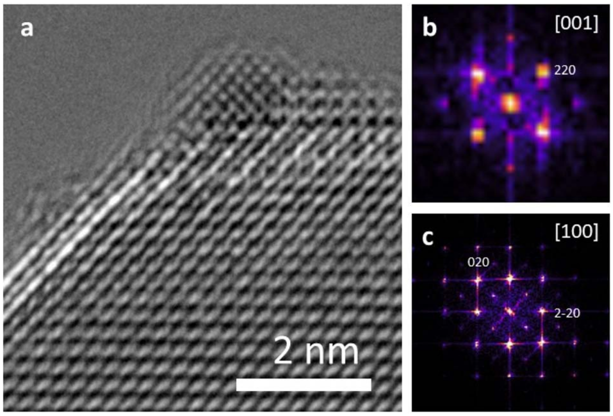

Fig. 9 (a) Aberration corrected HRTEM of platinum nanoparticle grafted onto STO. Fast Fourier transform patterns of the (b) platinum nanoparticle and (c) STO indicating the orientation and cube-on-cube epitaxial growth. The purple color in (b) and (c) is the result of both noise and overlapping intensities in the diffraction pattern. The white and yellow points in these sub-figures were used to determine which Pt and STO facets were imaged.

synthesized by ALD show a larger relative amount of cube-on-cube epitaxy in comparable samples,[24,26,92] these results are generally consistent with observations that smaller average sizes for deposited nanoparticles lead to distortions in epitaxial stabilization.[92,93] Such distortions include but are not limited to planar epitaxy, as is the case here, or existences as twinned particles, as was observed in some images corresponding to the experiment in Fig. 9. An example of such epitaxy is presented in the ESI (Fig. S12†).

Catalytic testing and recyclability

The 2cPt_red/STO was tested in the hydrogenolysis of i-PP at 300 °C and 180 psi for 24 h. The sample was chosen because its Pt loading and average Pt particle diameter most closely match Pt/STO catalysts synthesized by one cycle of ALD,[18,23] allowing comparison of hydrogenolysis results between physically similar samples. The yield of liquid products was 96.3%. The M_n of the product was ~270 Da with a dispersity ($Đ$) of 1.1 (Fig. 10). A key feature of the ALD-Pt/STO is its reusability, which is a result of its stability against sintering, as determined by repeated catalytic tests and TEM of the post-reaction catalyst. The 2cPt_red/STO was recovered and used four additional times for a total of five catalytic runs, and full conversion of i-PP was obtained for all runs (no solid product remained). The M_n of the product was obtained from the used 2cPt_red/STO catalyst was identical to the first experiment with fresh catalyst. There were a few changes in hydrogenolysis experiments over catalyst recycling. First, the molar H_2 consumption, corresponding to the moles of C–C bonds that are hydrogenolyzed, was 3.0 mmol for the first run and approximately 4 mmol for subsequent runs, with less than 10% of the i-PP converted (Fig. S13†). There was a small decrease in the quantity of methane formed after the first two runs, which may be related to changes in the available active sites. After the first catalytic run, the headspace is comprised of around 70 mol% methane. An equivalent mole percent of methane formation was reported by Hackler *et al.*, who used a comparable Pt/STO catalyst for i-PP upcycling under largely equivalent conditions.[21]

After the 5 consecutive catalytic runs, Pt particle size increased slightly from 1.2 nm to 1.8 nm (Fig. 11a and b) and the Pt loading increased from 1.082 to 1.204 wt%, likely because of the loss of carbon-rich species from the as-prepared catalyst. However, the Pt/Ti ratio decreased only slightly from 0.0446 to 0.0443, indicating a negligible loss of Pt.

The 2cPt_cal+red/STO catalyst, containing smaller nanoparticles, was also tested for stability against sintering by repeated catalytic testing for i-PP hydrogenolysis at 300 °C, 180 psi for 24 h. The M_n of the product was ~200 Da for the first 4

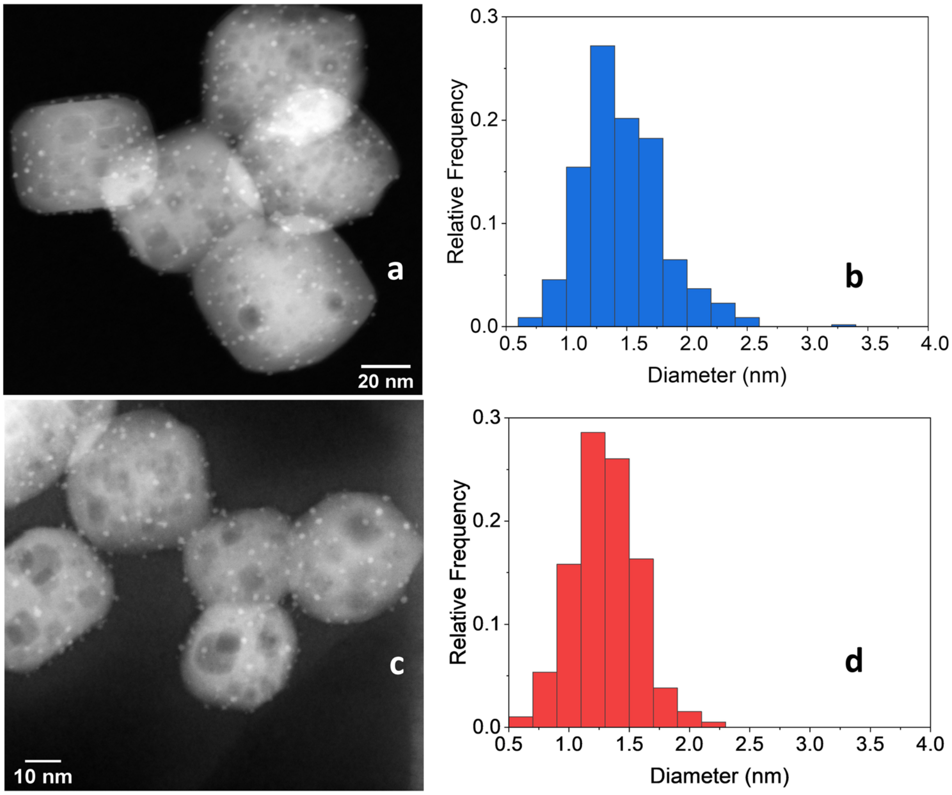

Fig. 11 (a) STEM-HAADF image of 2cPt/STO and (b) platinum particle size distributions (1.8 ± 0.89 nm) (right) after 5 catalytic runs. The initial sample is 2cPt_red/STO (Table 1). (c) STEM-HAADF image of 2cPt/STO and (d) platinum particle size distributions (1.3 ± 0.49 nm) after 5 catalytic runs. The initial sample is 2cPt_cal+red/STO (Table 1).

runs and 218 Da after the 4th run (Fig. 12). More light gases, in particular methane, and liquid alkanes (C_5H_{12} and C_6H_{14}) were formed after initial runs, although the amounts of gases and liquids formed decreased with successive reactions (Fig. S14†).

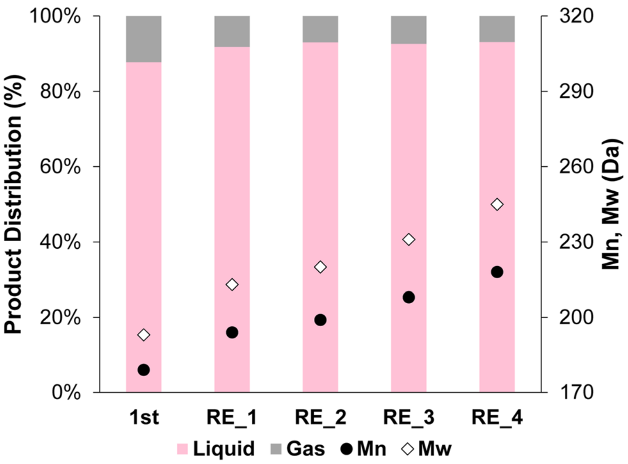

Fig. 12 Product distribution (liquid and gas) and M_n and M_w from OL after the first hydrogenolysis and 4 consecutive recycling experiments using 2cPt_cal+red/STO. Conditions: i-PP (3 g), 301.0 mg 2cPt_cal+red/STO catalyst, 300 °C, 180 psi mixed gas, 24 h. For gas distribution, see ESI.† No solid products were observed. $Đ = 1.1$ for all.

It was previously proposed that smaller catalyst nanoparticles produce lower molecular-weight upcycling products due to the availability of more Pt edge sites, which may be active sites for polymer hydrogenolysis, potentially explaining the greater methane production. The particle sizes reported above are consistent with this relative definition of "smaller" particles.[18] Pictures of the initial polymer and final products are presented in Fig. S15.† In general, the SOMC-derived Pt/STO catalyst reported herein hydrogenolyzes polyolefins to upcycled products with similar yields and average molecular weights to those made by comparable catalysts, such as those reported by Hackler.[20,21] A table of comparable catalysts is presented in the ESI (Table S3†). After the 5 consecutive catalytic runs, Pt particle size increased slightly from 1.0 nm to 1.3 nm (Fig. 11c and d) and the Pt loading increased from 0.936 to 0.960 wt%. However, the Pt/Ti ratio decreased only slightly from 0.0374 to 0.0214, also indicating a negligible loss of Pt.

XAFS was performed on the fresh and spent 2cPt_red/STO and 2cPt_cal+red/STO. According to the Pt L3 XANES, the 2cPt_cal+red/STO was the least reduced sample while the two spent samples were the most reduced (Fig. S16†) by qualitative comparison of the spectra with Pt metal and PtO_2. Linear combination fitting (LCF) with the metal and oxide spectra for the fresh samples indicates a larger fraction of oxidized Pt in 2cPt_cal+red/STO than 2cPt_red (Table S4†), consistent with

Table 2 Pt L3 edge EXAFS fit results for 2cPt/STO samples before and after 5 reactions ($k = 3.0–15$ Å^{-1}, $\Delta k = 0.5$, k^N $N = 1, 2, 3$, $R = 1.9–3.1$ Å). $S_0{}^2$ set to the value (0.84) fit for the Pt reference foil. Notation: N – coordination number, R – distance to neighboring atom, σ^2 – Debye–Waller factor, ΔE_0 – energy correction

Sample		N	R (Å)	σ^2 ($\times 10^{-3}$ Å^2)	ΔE_0 (eV)	R-Factor
2cPt_red/STO	Fresh	8.5 ± 0.4	2.727 ± 0.002	7.5 ± 0.3	5.8 ± 0.4	0.004
	Spent	8.6 ± 0.4	2.737 ± 0.002	6.6 ± 0.3	5.6 ± 0.4	0.004
2cPt_cal+red/STO	Fresh	8.2 ± 0.8	2.711 ± 0.006	9.5 ± 0.7	5.0 ± 0.3	0.020
	Spent	7.7 ± 0.4	2.716 ± 0.003	8.2 ± 0.3	4.3 ± 0.4	0.004
Pt metal	—	12	2.765 ± 0.002	4.8 ± 0.2	7.6 ± 0.4	0.008

smaller average particle sizes observed for the former (Table 1). Spent 2cPt_red and 2cPt_cal+red/STO closely resemble metallic Pt even after air exposure (Fig. S16†), suggesting surface species deposited from the hydrogenolysis experiments may have prevented re-oxidation of surface Pt unlike the fresh materials. After an *in situ* reduction in 3.5% H_2/He at 250 °C for 10 min, all samples were reduced (Fig. S17†). For both samples, there was no significant change in the Pt–Pt coordination number (Table 2) after reaction, although larger Pt–Pt bond lengths and smaller Debye–Waller factors fit for the spent samples also support an increase in the average Pt particle size following hydrogenolysis for both 2cPt_cal+red/STO and 2cPt_red. The sample that was calcined first had a lower coordination number (8.2 *vs.* 8.5) and Pt–Pt bond length than the sample reduced without calcination which is also in agreement with a smaller particle size observed in TEM and suggested from XANES LCF results (Table S4†).

Conclusions

In this work, we have established a multi-cycle, SOMC-derived process by which Pt/STO catalysts can be synthesized from organometallic Pt precursors in a toluene solution. Prior to deposition, the STO support surface is calcined, ozonolysed, and steamed at 200 °C. $MeCpPtMe_3$ and $Pt(acac)_2$ were both grafted onto STO in toluene, and $Pt(acac)_2$ was found to afford a significantly higher Pt loading. Deposition of $Pt(acac)_2$ at 80 °C was found to be optimal because it produced the highest Pt loading and best homogeneity after surface decoration. This afforded samples with average Pt particle sizes of 1.3, 1.2, and 1.5 nm, corresponding to Pt loadings of 0.6 wt%, 1.1 wt%, and 1.6 wt% after 1, 2, and 3 cycles of deposition and reduction in H_2, respectively. These data suggest that SOMC techniques, when applied in successive cycles, favor new particle deposition over increasing the size of existing particles.

Two samples of 2cPt/STO, one which was reduced and another which was both calcined and reduced after synthesis, were tested for hydrogenolysis of isotactic polypropylene ($M_n = 5$ kDa, $M_w = 12$ kDa). The Pt/STO samples have average Pt particle sizes of around 1.2 and 1.0 nm, respectively, and afforded final upcycling products (all >95% yield) with molecular weights around 300 and 200 Da, respectively. This suggests that smaller supported Pt nanoparticles are generally more active for polyolefin hydrogenolysis, which is consistent with previous reports of plastic upcycling with the Pt/STO system. Overall, the results suggest that SOMC-derived Pt/STO catalysts meet several proof-of-concept criteria and have the potential to be commercially viable upcycling catalysts.

Conflicts of interest

There are no conflicts to declare.

Acknowledgements

This work was supported as part of the Institute for Cooperative Upcycling of Plastics (iCOUP), an Energy Frontier Research Center funded by the U.S. Department of Energy, Office of Science, Basic Energy Sciences. This work was also partially supported by DOE/EERE/AMO and BETO for studies of catalytic hydrogenolysis of plastic waste (Award Number DE-EE0009300). Argonne National Laboratory is operated by UChicago Argonne LLC under Contract DE-AC-02-06CH11357 for the United States Department of Energy, and Ames Laboratory is operated by Iowa State University under Contract DE-AC-02-07CH11358 for the United States Department of Energy. The authors acknowledge the Materials Engineering Research Facility (MERF) at Argonne National Laboratory for synthetic contributions in the large-scale batch synthesis of STO nanocuboid supports. Use of the Advanced Photon Source is supported by the U.S. Department of Energy, Office of Science, and Office of the Basic Energy Sciences, under Contract No. DE-AC-02-06CH11357. MRCAT operations at Sector 10 are supported by the Department of Energy and the MRCAT member institutions. The EPR work at Argonne National Laboratory was supported by the U.S. Department of Energy (DOE), Office of Science, Office of Basic Energy Sciences, Division of Chemical Sciences, Geosciences, and Biosciences, under Contract No. DE-AC-02-06CH11357. Work performed at the Center for Nanoscale Materials including ACAT and Talos, a U.S. Department of Energy Office of Science User Facility, was supported by the U.S. DOE, Office of Basic Energy Sciences, under Contract No. DE-AC02-06CH11357. This work also made use of (i) the EPIC and Bio-Cryo facilities of Northwestern University's NUANCE Center, which has received support from the Soft and Hybrid Nanotechnology Experimental (SHyNE) Resource (NSF ECCS-1542205); the MRSEC program (NSF DMR-1720139) at the Materials Research Center; the International Institute for Nanotechnology (IIN); the Keck Foundation; and the State of Illinois, through the IIN, (ii) CryoCluster equipment, which has received support from the MRI program (NSF DMR-1229693), and (iii) Jerome B. Cohen X-ray Diffraction Facility supported by the MRSEC program of the National Science Foundation (DMR-1720139) at the Materials Research Center of Northwestern University and the Soft and Hybrid Nanotechnology Experimental (SHyNE) Resource (NSF ECCS-1542205). The authors thank Dr Uddhav Kanbur for synthetic contributions, Dr Ahmed Farghaly for helpful discussions, and Dr Long Qi for the development and use of UPLC to analyze molecular weights of liquid samples.

References

1 R. Gaye, J. R. Jambeck and K. L. Law, *Sci. Adv.*, 2017, **3**(7), e1700782.

2 A. L. Andrady, *Mar. Pollut. Bull.*, 2011, **62**, 1596–1605.

3 D. Eerkes-Medrano, R. C. Thompson and D. C. Aldridge, *Water Res.*, 2015, **75**, 63–82.

4 J. M. Garcia and M. L. Robertson, *Science*, 2017, **358**, 870–872.

5 S. B. Borrelle, J. Ringma, K. Law, C. C. Monnahan, L. Lebreton, A. McGivern, E. Murphy, J. R. Jambeck, G. H. Leonard, M. A. Hilleary, M. Eriksen, H. P. Possingham, H. De Frong, L. R. Gerber, B. Polidoro, A. Tahir, M. Bernard, N. Mallos, M. Barnes and C. M. Rochman, *Science*, 2020, **369**, 1515–1518.

6 L. Lebreton and A. Andrady, *Palgrave Communications*, 2019, **5**, 6.

7 S. M. Al-Salem, A. Antelaya, G. Constantinou, A. Manos and J. Dutta, *Environ. Manage.*, 2017, **197**, 177–198.

8 K. V. Popov and V. D. Knyazev, *J. Phys. Chem. A*, 2015, **119**, 11737–11760.

9 S. E. Levine and L. J. Broadbelt, *Polym. Degrad. Stab.*, 2009, **94**, 810–822.

10 G. Lopez, M. Artetxe, M. Amutio, J. Bilbao and M. Olazar, *Renewable Sustainable Energy Rev.*, 2017, **73**, 346–368.

11 P. A. Kots, B. C. Vance and D. G. Vlachos, *React. Chem. Eng.*, 2022, **7**, 41–54.

12 B. C. Vance, P. A. Kots, C. Wang, Z. R. Hinton, C. M. Quinn, T. H. Epps, L. T. J. Korley and D. G. Vlachos, *Appl. Catal., B*, 2021, **299**, 120483.

13 F. Zhang, M. Zeng, R. D. Yappert, J. Sun, Y. H. Lee, A. M. LaPointe, P. Peters, M. M. Abu-Omar and S. L. Scott, *Science*, 2020, **370**, 437–441.

14 A. Tennakoon, X. Wu, A. L. Paterson, S. Patnaik, Y. Pei, A. M. LaPoint, S. C. Ammal, R. A. Hackler, A. Heyden, I. I. Slowing, G. W. Coates, M. Delferro, B. Peters, W. Huang, A. D. Sadow and F. A. Perras, *Nat. Catal.*, 2020, 893–908.

15 J. E. Rorrer, G. T. Beckham and Y. Román-Leshkov, *JACS Au*, 2021, **1**, 8–12.

16 Y. Nakaji, M. Tamura, S. Miyaoka, S. Kumagai, M. Tanji, Y. Nakagawa, T. Yoshioka and K. Tomishige, *Appl. Catal., B*, 2021, **286**, 119805.

17 J. E. Rorrer, C. Troyano-Valls, G. T. Beckham and Y. Román-Leshkov, *ACS Sustainable Chem. Eng.*, 2021, **9**, 11661–11666.

18 G. Celik, R. M. Kennedy, R. A. Hackler, M. Ferrandon, A. Tennakoon, S. Patnaik, A. M. LaPointe, S. C. Ammal, A. Heyden, F. A. Perras, M. Pruski, S. L. Scott, K. R. Poeppelmeier, A. D. Sadow and M. Delferro, *ACS Cent. Sci.*, 2019, **5**, 1795–1803.

19 I. L. Peczak, R. M. Kennedy, R. A. Hackler, Y. Shin, M. Delferro and K. R. Poeppelmeier, *ACS Appl. Mater. Interfaces*, 2021, **13**(49), 58691–58700.

20 R. A. Hackler, K. Vyayhare, R. M. Kennedy, G. Celik, U. Kanbur, P. J. Griffin, A. D. Sadow, G. Zang, A. Elgowainy, P. Sun, K. R. Poeppelmeier, A. Erdemir and M. Delferro, *ChemSusChem*, 2021, **14**, 4181–4189.

21 R. A. Hackler, J. V. Lamb, I. L. Peczak, R. M. Kennedy, A. M. LaPointe, K. R. Poeppelmeier, A. D. Sadow and M. Delferro, *Macromolecules*, 2022, **55**(15), 6801–6810.

22 V. Capello, P. Sun, G. Zang, S. Kumar, R. A. Hackler, H. E. Delgado, A. Elgowainy, M. Delferro and T. Krause, *Green Chem.*, 2022, **24**, 6306–6318.

23 S. T. Christensen, J. W. Elam, F. A. Rabuffetti, Q. Ma, S. J. Weigand, B. Lee, S. Seifer, P. C. Stair, K. R. Poeppelmeier, M. C. Hersam and M. J. Bedzyk, *Small*, 2009, **5**(6), 750–757.

24 Y. Lin, J. Wen, L. Hu, R. M. Kennedy, P. C. Stair, K. R. Poeppelmeier and L. D. Marks, *Phys. Rev. Lett.*, 2013, **111**, 156101.

25 J. A. Enterkin, W. Setthapun, J. Elam, S. T. Christensen, F. A. Rabuffetti, L. D. Marks, P. C. Stair, K. R. Poeppelmeier and C. L. Marshall, *ACS Catal.*, 2011, **1**, 629–635.

26 J. Enterkin, K. R. Poeppelmeier and L. D. Marks, *Nano Lett.*, 2011, **11**, 993–997.

27 Y. Yang, D. Zhang, W. Ji, F. Bi, L. Song and X. Zhang, *J. Colloid Interface Sci.*, 2022, **606**, 1811–1823.

28 P. Munnik, P. E. de Jongh and K. P. de Jong, *Chem. Rev.*, 2015, **115**(14), 6687–6718.

29 V. M. Koch, M. K. S. Barr, P. Buttner, I. Minguez-Bacho, D. Dohler, B. Winzer, E. Reinhardt, D. Segets and J. Bachmann, *J. Mater. Chem. A*, 2019, **7**, 25112–25119.

30 J. Fitchner, Y. Wu, J. Hitzenberger, T. Drewello and J. Bachmann, *J. Solid State Sci. Technol.*, 2017, **6**(9), N171–N175.

31 B. P. Le Monnier, F. Wells, F. Talebkeikhah and J. S. Luterbacher, *Adv. Mater.*, 2019, **31**(52), 1904276.

32 S. P. Zankowski, L. van Hoecke, F. Mattelaer, M. de Raedt, O. Richard, C. Detavernier and P. M. Vereecken, *Chem. Mater.*, 2019, **31**(13), 4805–4816.

33 Y. Wu, D. Dohler, M. Barr, E. Oks, M. Wolf, L. Santinacci and J. Bachmann, *Nano Lett.*, 2015, **15**(10), 6379–6385.

34 R. J. Witzke, A. Chaptoevsky, M. P. Conley, D. M. Kaphan and M. Delferro, *ACS Catal.*, 2020, **10**(20), 11822–11840.

35 M. Stalzer, M. Delferro and T. J. Marks, *Catal. Lett.*, 2015, **145**, 3–14.

36 C. Coperet, A. Comas-Vives, M. P. Conley, D. P. Estes, A. Fedorov, V. Mougel, H. Nagae, F. Nuñez-Zarur and P. Zhizhko, *Chem. Rev.*, 2016, **116**, 323–421.

37 J. D. A. Pelletier and J. M. Basset, *Acc. Chem. Res.*, 2016, **49**, 664–677.

38 C. Coperet, A. Federovo and P. A. Zhizhko, *Catal. Lett.*, 2017, **147**, 2247–2259.
39 C. Coperet, F. Allouche, K. W. Chan, M. P. Conley, M. F. Delley, A. Fedorov, I. B. Moroz, V. Mougel, M. Pucino, K. Searles, K. Yamamoto and P. A. Zhizhko, *Angew. Chem., Int. Ed.*, 2018, **57**, 6398–6440.
40 M. S. Ferrandon, C. Byron, G. Celik, Y. Zhang, C. Ni, J. Sloppy, R. A. McCormick, K. Booksh, A. V. Teplyakov and M. Delffero, *Appl. Catal., A*, 2022, **629**, 118379.
41 K. R. Poeppelmeier, T. D. Trowbridge and J.-L. Kao, *US Pat.*, 4568656, February 4, 1986.
42 S. J. Tauster, A. A. Montagna, J. J. Steger, S. C. Fung and V. R. Cross, *US Pat.*, 4634517, January 6, 1987.
43 S. J. Tauster and J. J. Steger, *J. Catal.*, 1990, **125**, 387–389.
44 J. P. Marques, I. Gener, P. Ayrault, J. C. Bordado, J. M. Lopes, F. Ramôa Ribeiro and M. Guisnet, *Microporous Mesoporous Mater.*, 2003, **1**(60), 251–262.
45 I. Batonnaeu-Gener, A. Yonli, S. Hazael-Pascal, J. Pedro Marques, J. Madeira Lopes, M. Guisnet, F. Ramôa Ribeiro and S. Mignard, *Microporous Mesoporous Mater.*, 2008, **110**(2), 480–487.
46 H. Son, S. J. Lee, A. Soon, H.-S. Roh and H. Lee, *Appl. Catal., B*, 2013, **134**, 103–109.
47 R. R. Shrock, *J. Organomet. Chem.*, 1976, **122**(2), 209–225.
48 A. Zagdoun, G. Casano, O. Ouari, M. Schwarzwalder, A. J. Rossini, F. Aussenac, M. Yulikov, G. Jeschke, C. Copéret, A. Lesage, P. Tordo and L. Emsley, *J. Am. Chem. Soc.*, 2013, **135**(34), 12790–12797.
49 F. A. Perras, T. Kobayashki and M. Pruski, *J. Am. Chem. Soc.*, 2015, **137**(26), 8336–8339.
50 X. Zhao, W. Hoffbauer, J. S. auf der Gunne and M. H. Levitt, *Solid State Nucl. Magn. Reson.*, 2004, **26**(2), 57–64.
51 H. Nagashima, J. Trébosc, Y. Kon, K. Sato, O. Lafon and J.-P. Amoureux, *J. Am. Chem. Soc.*, 2020, **142**(24), 10659–10672.
52 F. A. Perras, K. C. Boteju, I. I. Slowing, A. D. Sadow and M. Pruski, *Chem. Commun.*, 2018, **54**, 3472–3475.
53 F. H. Larsen, J. Skibsted, H. J. Jakobsen and N. C. Nielsen, *J. Am. Chem. Soc.*, 2000, **122**(29), 7080–7086.
54 A. Bielecki, A. C. Kolbert and M. H. Levitt, *Chem. Phys. Lett.*, 1989, **155**(4–5), 341–346.
55 A. Venkatesh, D. Gioffre, B. A. Atterberry, K. Rochlitz, S. L. Carnahan, Z. Wang, G. Menzildjian, A. Lesage, C. Copéret and A. J. Rossini, *J. Am. Chem. Soc.*, 2022, **144**(30), 13511–13525.
56 S. J. Clark, M. D. Segall, C. J. Pickard, P. J. Hasnip, M. I. J. Probert and K. Refson, *Zeitschrift für Kristallographie – Crystalline Materials*, 2005, **220**, 567–570.
57 D. Vanderbilt, *Phys. Rev. B: Condens. Matter Mater. Phys.*, 1990, **41**, 7892–7895.
58 J. P. Perdew, K. Burke and M. Ernezkhof, *Phys. Rev. Lett.*, 1996, **77**, 3865–3868.
59 S. Grimme, *Comput. Chem.*, 2006, **27**(15), 1787–1799.
60 C. J. Pickard and F. Mauri, *Phys. Rev. B: Condens. Matter Mater. Phys.*, 2001, **63**, 245101.
61 J. R. Yates, C. J. Pickard and F. Mauri, *Phys. Rev. B: Condens. Matter Mater. Phys.*, 2007, **76**, 024401.
62 W. S. Rasband, *ImageJ*, U. S. National Institutes of Health, Bethesda, Maryland, USA, 1997–2018, https://imagej.nih.gov/ij/.
63 (*a*) B. Ravel and M. Newville, *J. Synchrotron Radiat.*, 2005, **12**, 537–541; (*b*) T. B. Bolin, T. Wu, N. Schweitzer, R. Lobo-Lapidus, A. J. Kropf, H. Wang, Y. Hu, J. T. Miller and S. M. Heald, *Catal. Today*, 2013, **205**, 141–147.
64 F. A. Rabuffetti, H.-S. Kim, J. A. Enterkin, Y. Wang, C. H. Lanier, L. D. Marks and K. R. Poeppelmeier, *Chem. Mater.*, 2008, **20**, 5628–5635.
65 T. K. Andersen, D. D. Fong and L. D. Marks, *Surf. Sci. Rep.*, 2018, **73**, 213–232.
66 L. A. Crosby, B.-R. Chen, R. M. Kennedy, J. Wen, K. R. Poeppelmeier, M. J. Bedzyk and L. D. Marks, *Chem. Mater.*, 2018, **30**, 841–846.
67 D. M. Kienzle and L. D. Marks, *CrystEngComm*, 2012, **14**, 7833–7839.
68 L. D. Marks and L. Peng, *J. Phys.: Condens. Matter*, 2016, **28**, 053001.
69 L. Crosby, J. Enterkin, F. A. Rabuffetti, K. R. Poeppelmeier and L. D. Marks, *Surf. Sci.*, 2015, **632**, L22–L25.
70 L. Bai, F. Polo-Garzon, Z. Bao, S. Luo, B. M. Moskowitz, H. Tian and Z. Wu, *ChemCatChem*, 2019, **11**, 2107–2117.
71 G. S. Foo, Z. D. Hood and Z. Wu, *ACS Catal.*, 2018, **8**(1), 555–565.
72 Z. Bao, V. Fung, F. Polo-Garzon, Z. D. Hood, S. Cao, M. Chi, L. Bai, D. Jiang and Z. Wu, *J. Catal.*, 2020, **384**, 49–60.
73 Z. Zhang, L. Li and J. C. Yang, *J. Phys. Chem. C*, 2013, **117**, 21407–21412.
74 F. Grillo, H. Vanbui, D. La Zara, A. A. I. Arnink, A. Y. Kovalgin, P. Kooyman, M. T. Kreutzer and J. R. van Ommen, *Small*, 2018, **14**, 1800765.
75 M. M. Lencka and R. E. Riman, *Chem. Mater.*, 1993, **5**, 61–70.
76 M. M. Lencka and R. E. Riman, *Chem. Mater.*, 1995, **7**(1), 18–25.
77 M. M. Lencka and R. E. Riman, *Ferroelectrics*, 1994, **151**, 159–164.
78 M. Crespin and W. K. Hall, *J. Catal.*, 1981, **69**(2), 359–370.
79 (*a*) N. Domingo, E. Pach, K. Cordero-Edward, V. Pérez-Dieste, C. Escudero and A. Veradguer, *Phys. Chem. Chem. Phys.*, 2019, **21**(9), 4920–4930; (*b*) A. E. Becerra-Toledo, J. A. Enterkin, D. M. Kienzle and L. D. Marks, *Surf. Sci.*, 2012, **606**(9–10), 791–802.
80 A. E. Becerra-Toledo, M. R. Castell and L. D. Marks, *Surf. Sci.*, 2012, **606**(7–8), 762–765.
81 D. M. Kienzle, A. E. Becerra-Toledo and L. D. Marks, *Phys. Rev. Lett.*, 2011, **106**, 176102.
82 D. Astruc, *Nanoparticles and Catalysis*, Wiley-VCH, Weinheim, 2008.
83 B. K. Hodnett, *Heterogeneous Catalytic Oxidation*, Wiley, West Sussex, 2000.
84 C. Dossi, R. Pasro, A. Bartsch, E. Brivio, A. Galadsco and P. Losi, *Catal. Today*, 1993, **17**, 527–535.
85 H. Miura, *Catal. Today*, 1996, 215–221.
86 W. Setthapun, W. D. Williams, S. M. Kim, H. Feng, J. W. Elam, F. A. Rabuffetti, K. R. Poeppelmeier, P. C. Star,

E. A. Stach, F. H. Ribeiro, J. T. Miller and C. L. Marshall, *J. Phys. Chem. C*, 2010, **21**, 9758–9771.

87 J. Camacho-Bunquin, M. Ferrandon, H. Sohn, D. Yang, C. Liu, P. A. Ignacio-de-Leon, F. A. Perras, M. Pruski, P. C. Stair and M. Delferro, *J. Am. Chem. Soc.*, 2018, **140**(11), 3940–3951.

88 A. Jentys, *Phys. Chem. Chem. Phys.*, 1999, **1**, 4059–4063.

89 M. S. Martín González, M. H. Aguirre, E. Morán, M. Á. Alario-Franco, V. Perez-Dieste, J. Avila and M. C. Asensio, *Solid State Sci.*, 2000, **2**, 519–524.

90 F. Grillo, H. Van Bui, D. La Zara, A. A. I. Aarnink, A. Y. Kovalgin, P. Kooyman, M. T. Kreutzer and J. R. van Ommen, *Small*, 2018, **14**, 1800765.

91 G. Bergeret and P. Gallezot, Particle Size and Dispersion Measurement, in *Handbook of Heterogeneous Catalysis*, 2008, pp. 738–765.

92 A. Enterkin, R. M. Kennedy, J. Lu, J. W. Elam, R. E. Cook, L. D. Marks, P. C. Stair, C. L. Marshall and K. R. Poeppelmeier, *Top. Catal.*, 2013, **56**, 1829–1834.

93 J. R. Gallagher, T. Li, H. Zhao, J. Liu, Y. Lei, X. Zhang, Y. Ren, J. W. Elam, R. J. Meyer and R. E. Winans, *Catal. Sci. Technol.*, 2014, **4**(9), 3053–3063.